Simulation of Lateral Near- and Far-Field Profiles of Gain-Guided High-Power Semiconductor Lasers

Carlo Holly and Stewart McDougall
TRUMPF Photonics, Inc.
2601 Route 130 South, Cranbury, NJ 08512, USA
Email: carlo.holly@trumpf.com

***Abstract*—The objective of this paper is to present the simulation of the lateral emission characteristics of broad-area diode lasers by the example of two devices which differ in contact width, and demonstrate that the applied model is capable to predict far-field divergence and near-field width over current. The numerical results are compared to experimental data.**

***Index Terms*—Semiconductor Lasers, Diode Lasers, Lasers, Simulation, Modeling, Broad-Area, Gain-Guided, Beam Propagation Method, Frequency Domain**

I. INTRODUCTION

Pump applications and direct applications demand High-Power Diode Lasers (HPDLs) with high brightness and reliability. The Slow-Axis Divergence (SAD) over current for gain-guided devices is mainly influenced by the spatial carrier- and temperature distribution. The trend is characterized by a substantial increase in SAD with increasing current. This thermally induced beam quality deterioration can be shifted to higher currents with an increase in the emitter width or length in conjunction with lower dissipated power and temperature. The objective of this paper is to present the simulation of this effect by the example of two SE devices, which differ only in contact width, and demonstrate that the applied model is capable to predict lateral emission characteristics of HPDLs. The results presented in this paper are published in the thesis [1].

II. MODEL

The frequency-domain edge-emitting laser model, as presented in [1] is utilized to determine the optical field and interaction with the semiconductor medium. The electric field is propagated along the cavity between transverse slices in a Fox-Li iteration using the Finite-Differences Beam-Propagation Method (FD-BPM). During the iteration, material parameters, including local gain, refractive index perturbations and temperature are updated consistently. For details about the model and additional simulation results refer to [1]. Iterative models similar to the one applied here are reported also in the literature in [2], [3] and others. The filamentation of the light field mainly emerges from perturbations of the refractive index due to the density of carriers N, and the temperature profile T, see Fig. 1. In the model, the effective refractive index at frequency ω is updated between transverse slices based on $n_{\mathrm{eff}}(\omega, N, T) = n_{\mathrm{eff},0} + \Gamma\delta n_N(N) + \delta n_T(T) \approx n_{\mathrm{eff},0} + \Gamma\alpha_N\Delta N + \alpha_T\Delta T$, where $n_{\mathrm{eff},0}$ is the background effective refractive index and Γ is the optical confinement factor. The refractive index changes δn_N and δn_T are approximated by linear dependencies. A value of $3 \times 10^{-4}\,\mathrm{K}^{-1}$ is applied for the coefficient of the modal thermal-induced refractive index change of lasers with AlGaAs waveguides in [4], and a value of $4.9 \times 10^{-4}\,\mathrm{K}^{-1}$ is reported in [5]. In this study, the parameters α_T and α_N are adjusted, so that the measured FF and NF widths of the device D1 match with the simulation. The calibration results in $\alpha_T = 4 \times 10^{-4}\,\mathrm{K}^{-1}$ and $\alpha_N = -1.7 \times 10^{-26}\,\mathrm{m}^3$. For a quantitative comparison between the calculated and measured Far-Field (FF) and Near-Field (NF), the total dissipated power (for the individual device) is extracted from measurements and the heat sources obtained in the simulation are re-scaled so that the total power matches the measured dissipated power. This step is performed to circumvent uncertainties in the prediction of the electro-optical efficiency and to ensure a thermal profile close to the one in the real device. The parameters used in the model are, the optical confinement factor $\Gamma = 0.721\%$, effective refractive index $n_{\mathrm{eff}} = 3.4$, gain coefficient $G_0 = 2.2 \times 10^5\,\mathrm{m}^{-1}$ (for logarithmic dependency), linearized thermal change of gain coefficient $G_{0,T} = -63\,\mathrm{m}^{-1}\mathrm{K}^{-1}$, transparency carrier density $N_{\mathrm{tr}} = 2 \times 10^{24}\,\mathrm{m}^{-3}$, linearized thermal change of transparency carrier density $N_{\mathrm{tr},T} = 1.01 \times 10^{22}\,\mathrm{m}^{-3}\mathrm{K}^{-1}$, contribution-factor of spontaneous emission $\beta_{\mathrm{sp}} = 1\mathrm{e}-3$, internal absorption $\alpha_{\mathrm{int}} = 20\,\mathrm{m}^{-1}$, non-radiative recombination time $\tau_{\mathrm{nr}} = 5\,\mathrm{ns}$ [3], coefficient of spontaneous emission $B_{\mathrm{sp}} = 1.4 \times 10^{-16}\,\mathrm{m}^3\mathrm{s}^{-1}$ [3], ambipolar diffusion coefficient $D_{n/p} = 19.6 \times 10^{-4}\,\mathrm{m}^2\mathrm{s}^{-1}$, back-facet reflectivity $R_0 = 0.98$, front-facet reflectivity $R_{\mathrm{l}} = 0.02$, lateral resolution $N_{y,\mathrm{sim.}} = 1024$, and the longitudinal resolution $N_{z,\mathrm{sim.}} = 4000$. The parameters changed between both simulations are the contact width, and the boundary coefficient for the heat-sink, which is $g_{\mathrm{hs}} = 0.55 \times 10^5\,\mathrm{Wm}^{-2}\mathrm{K}^{-1}$ for D1, and $g_{\mathrm{hs}} = 0.86 \times 10^5\,\mathrm{Wm}^{-2}\mathrm{K}^{-1}$ for D2.

III. RESULTS

The model is applied to calculate NF and FF widths together with output power and temperature over current for two single emitter devices with $4\,\mathrm{mm}$ long cavities and contact widths of $100\,\mu\mathrm{m}$ for device D1, and $150\,\mu\mathrm{m}$ for device D2. Both lasers have a single InGaAs Quantum Well (QW) embedded in an AlGaAs waveguide and emit at $950\,\mathrm{nm}$ wavelength. A comparison of measured and simulated lateral FF intensity

978-1-7281-1647-1/19/$31.00 ©2019 IEEE

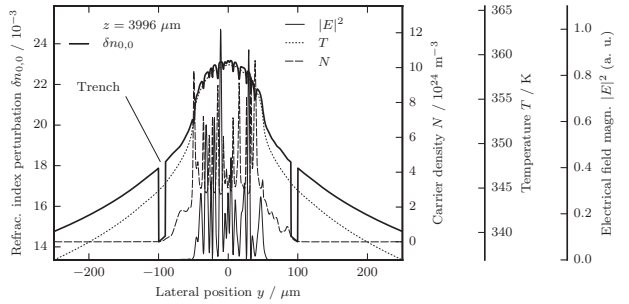

Fig. 1. Lateral profile of refractive index perturbation, carrier density, intensity and temperature for a current of 20 A at the front of the device. the snapshot is from round-trip 200 (plot from [1]).

profiles for device D1 is displayed in Fig. 2. The computed

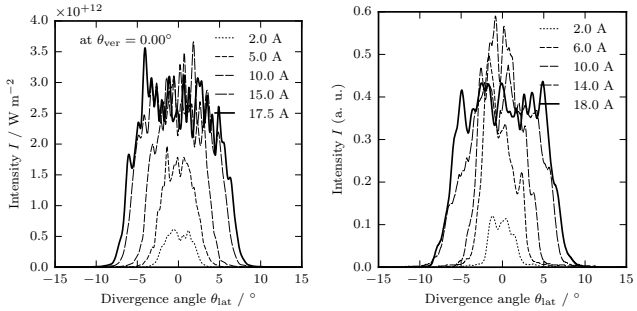

Fig. 2. Simulated (left) and measured (right) lateral FF profiles for various currents for a device with $100\,\mu$m contact opening and 4 mm cavity length. For the simulation results, the intensities are averaged over 50 round-trips (plot from [1]).

results for the D1 device are compared to three sets of measurements (Fig. 3), which in total amount to 37 tested devices. The increase in the slope of the SAD over current due to thermal lensing is reproduced. The measured NF widths for the filamented profiles show variations up to $\pm 10\,\mu$m between devices out of one set of measurements and offsets of the averaged NF widths up to $10\,\mu$m between data sets. The calculated output power matches the measured values, and the (averaged) temperature over current aligns with the measured one [1], which is a result of the adjustment of the heatsink coefficient for the thermal boundary condition. With the same parameters as used for D1, except for the change in the contact width to $150\,\mu$m and electro-optical efficiency (dissipated heat), the emission characteristics of device D2 are modeled. The dip in the SAD for D1 around 10 A is not observed for the wider device D2, and the increase of the SAD with current is reduced (Fig. 4). The lower thermal lensing also manifests in the trend of the NF width for D2. The contraction of the NF takes places at higher currents for D2 compared to D1.

IV. CONCLUSION

Among others, the calculation of the temperature on a three-dimensional domain, utilization of a wide-angle BPM, and fine tuning of simulation parameters significantly contribute to the

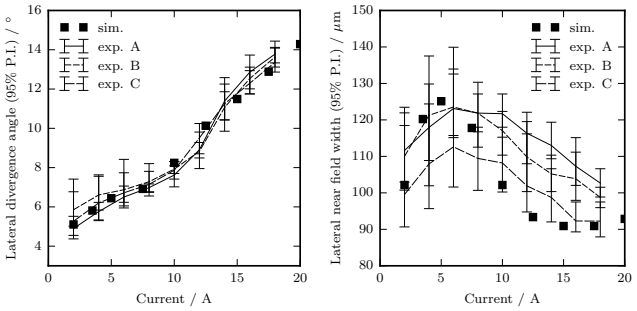

Fig. 3. Far-field divergence angle, near-field width, power and temperature over current for device D1 with $100\,\mu$m contact width (plot from [1]).

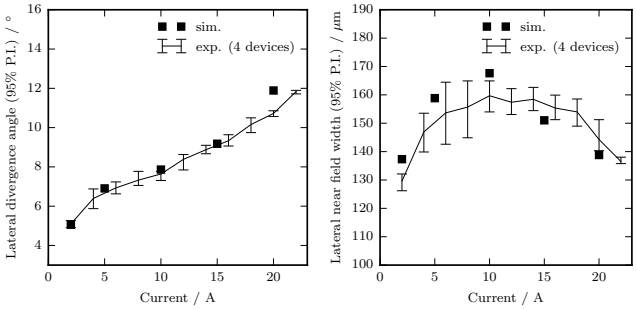

Fig. 4. Far-field divergence angle, near-field width, power and temperature over current for device D2 with $150\,\mu$m contact width (plot from [1]).

successful resemblance of the NF and FF profiles and widths of real devices by the numerical model. Differences in the trend of NF and FF widths over current are reproduced for a change in the contact opening width between $100\,\mu$m and $150\,\mu$m. Despite of the contact width and the total dissipated power over current (which is matched to the experiment) no parameters are changed between the simulations. The simulated NF widths lie within the range of the measured widths, although the NF narrowing for D1 for high currents seems to be slightly overestimated. The accurate reproduction of the emission profiles of real devices, which is presented here, is an advantage compared to the state-of-the-art and enables us to virtually design future devices for improvement of the brightness.

REFERENCES

[1] C. Holly, *Modeling of the Lateral Emission Characteristics of High-Power Broad-Area Edge-Emitting Semiconductor Lasers*. PhD thesis, Faculty of Mechanical Engineering, RWTH Aachen University, Aachen 2019 (to be published).

[2] J. J. Lim, et. al. "Design and Simulation of Next-Generation High-Power, High-Brightness Laser Diodes," *IEEE J. Sel. Topics Quantum Electron.*, vol. 15, pp. 993-1008, May 2009.

[3] J. R. Marciante and G. P. Agrawal, "Nonlinear Mechanisms of Filamentation in Broad-Area Semiconductor Lasers," *IEEE J. Quantum Electron.*, vol. 32, pp. 590-596, April 1996.

[4] J. Piprek, "Inverse Thermal Lens Effects on the Far-Field Blooming of Broad Area Laser Diodes," *IEEE Photon. Technol. Lett.*, vol. 25, pp. 958-960, May 2013.

[5] T. Paoli, "Waveguiding in a stripe-geometry junction laser," *IEEE J. Quantum Electron.*, vol. 13, pp. 662-668, August 1977.